Editors' Suggestion

Fermi surface topology and magnetotransport properties of superconducting $Pd_3Bi_2Se_2$

Ramakanta Chapai,[1,*] Gordon Peterson,[1] M. P. Smylie,[1,2] Xinglong Chen,[1] J. S. Jiang,[1] David Graf,[3] J. F. Mitchell,[1] and Ulrich Welp[1]

[1]*Materials Science Division, Argonne National Laboratory, Lemont, Illinois 60439, USA*
[2]*Department of Physics and Astronomy, Hofstra University, Hempstead, New York 11549, USA*
[3]*National High Magnetic Field Laboratory, Tallahassee, Florida 32310, USA*

(Received 12 June 2024; revised 9 August 2024; accepted 13 August 2024; published 27 August 2024)

$Pd_3Bi_2Se_2$ is a rare realization of a superconducting metal with a nonzero Z_2 topological invariant. Here, we report the growth of high-quality single crystals of layered $Pd_3Bi_2Se_2$ with a superconducting transition at $T_c \approx 0.80$ K and upper critical fields of ∼10 and ∼5 mT for the in-plane and out-of-plane directions, respectively. Our density-functional theory (DFT) calculations reveal three pairs of doubly degenerate bands crossing the Fermi level, all displaying clear three-dimensional dispersion consistent with the overall low electronic anisotropy (<2). The multiband electronic nature of $Pd_3Bi_2Se_2$ is evident in magnetotransport measurements, yielding a sign-changing Hall resistivity at low temperatures. The magnetoresistance is nonsaturating and follows Kohler's scaling rule. We interpret the magnetotransport data in terms of open orbits that are revealed in the DFT-calculated Fermi surface. de Haas–van Alphen (dHvA) oscillation measurements using torque magnetometry on single crystals yield four frequencies for out-of-plane fields: $F_\alpha = 150 \pm 26$ T, $F_\beta = 293 \pm 10$ T, $F_\gamma = 375 \pm 20$ T, and $F_\eta = 1017 \pm 12$ T, with the low frequency dominating the spectrum. Through the measurement of angular-dependent dHvA oscillations and DFT calculations we identify the F_α frequency with an approximately ellipsoidal electron pocket centered on the L_2 point of the Brillouin zone. Lifshitz-Kosevich analysis of the dHvA oscillations reveals a small cyclotron effective mass $m^* = (0.11 \pm 0.02)m_0$ and a nontrivial Berry phase for the dominant orbit. The presence of nontrivial topology in a bulk superconductor positions $Pd_3Bi_2Se_2$ as a potential candidate for exploring topological superconductivity.

DOI: 10.1103/PhysRevB.110.075152

I. INTRODUCTION

Topological materials remain as a frontier in condensed-matter physics, owing to their fascinating physical properties. Specifically, topological insulators and topological superconductors are being extensively explored due to their potential applications in quantum computation and spintronic technologies [1–6]. Topological superconductors are envisioned to exist in materials that possess topologically nontrivial bands and a superconducting ground state [6–12]. To achieve such exotic states, various approaches have been employed including doping topological insulators [13–15], applying external pressure to topological systems [16,17], and fabricating heterostructures consisting of topological insulators and conventional superconductors [18–21]. However, superconductivity induced by chemical doping or pressure faces difficulties in achieving high superconducting volume fraction [17,19], and it can be challenging to fabricate an atomically sharp interface between two different materials [18–21]. An alternative approach to realizing topological superconductivity is to identify nontrivial topological bands within bulk superconductors [22–25], though materials in this category remain scarce [9,26]. Only a few candidates, such as the noncentrosymmetric $CePt_3Si$ [26] and orthorhombic UTe_2 [27] heavy-fermion superconductors, and the layered transition-metal chalcogenide superconductors, like centrosymmetric $PdTe_2$ [28,29] and noncentrosymmetric $PbTaSe_2$ [30], have shown promise. Joining these candidates, kagome superconductors AV_3Sb_5 (A = Cs, Rb, K) have recently been identified as having topologically nontrivial band structures with a nonzero Z_2 invariant [31,32].

In parallel, the topological properties and Fermi surfaces within the parkerite and shandite family of compounds with composition $T_3M_2X_2$ (T = Ni, Co, Rh, Pd, Pt; M = In, Sn, Pb, Bi; X = S, Se, Te) [33–40], have attracted considerable attention. Many of these ternary compounds, such as $Rh_3Bi_2Se_2$ and $Rh_3Bi_2S_2$, exhibit superconductivity and charge-density wave (CDW) order [33,34]. Other members, such as $Co_3Sn_2S_2$ and $Pd_3Bi_2S_2$, are known to host nontrivial topology [41–43]. However, the Fermi surface topology of superconducting parkerites remains poorly understood [33–40]. One such parkerite-type compound, $Pd_3Bi_2Se_2$, is a superconductor with $T_c \approx 1$ K, with its superconducting properties reported in polycrystalline samples [35], thin films [37], and nanoparticles [38]. Recently, a nonzero Z_2 topological invariant of monoclinic parkerite-type $Pd_3Bi_2Se_2$ has been proposed theoretically [42–46], and unusual magnetotransport attributed to two-dimensional fermions has been reported in thin-film samples [39]. A possible CDW transition has also been identified in low-pressure (∼0.15 GPa) measurements [47]. Nevertheless, a detailed understanding of the Fermi

*Contact author: rchapai@anl.gov

surface, which is a prerequisite for comprehending correlated electronic behavior, has not yet been reported for $Pd_3Bi_2Se_2$ [33–40,48,49].

Here, we present the synthesis of large high-quality single crystals of $Pd_3Bi_2Se_2$ and detail its superconducting characteristics, normal-state magnetotransport, and de Haas–van Alphen (dHvA) oscillations, to shed light on the electronic structure and Fermi surface (FS) topology. Superconductivity is observed in electrical resistivity with the onset of the transition at $T_c \approx 0.83$ K in zero field. The temperature dependence of the upper critical field, H_{c2} (T) exhibits a modest anisotropy of less than 2, with zero-temperature values for the in-plane and out-of-plane directions of 9.7 and 5.2 mT, respectively with corresponding large Ginzburg-Landau coherence lengths of 190 and 111 nm. The temperature variation of the penetration depth, based on tunnel diode oscillator (TDO) measurements, is consistent with a complete superconducting gap. In the normal state, we observed clear dHvA oscillations at fields above 10 T and at low temperatures (<60 K), from which four frequencies are identified: $F_\alpha = 150$, $F_\beta = 293$, $F_\gamma = 375$, and $F_\eta = 1017$ T, with the F_α frequency dominating the spectrum. Lifshitz-Kosevich analysis yields a small cyclotron effective mass ($m^* = 0.11m_0$) and a nontrivial, Berry phase ($\Phi_B \approx \pi$) for the dominant orbit. These results are corroborated by density-functional theory (DFT) calculations of the electronic structure, which reveal three doubly degenerate bands crossing the Fermi level. One of these bands results in a small, approximately ellipsoidal electron pocket centered on the L_2 point of the Brillouin zone with a cyclotron effective mass of $0.15m_0$ for a magnetic field applied perpendicular to the *ab* plane. The observed angular dependence of the F_α oscillations is well described using a model based on an ellipsoidal FS centered on the L_2 point and aligned with the D-D_2 direction in the Brillouin zone.

Multiple dHvA oscillation frequencies indicate multiple bands crossing the Fermi level. Indeed, the presence of multiple Fermi surface pockets is confirmed by the Hall resistivity measurements, which show nonlinear variation with the applied magnetic field. Despite the multiband nature, we observe nonsaturating magnetoresistance that follows Kohler's scaling rule remarkably well, implying transport may be dominated by a single band or single-scattering mechanism. Furthermore, our DFT calculations reveal a large three-dimensional Fermi surface sheet, supporting multiple open orbits that may account for the observed magnetotransport behavior and the overall low electronic anisotropy of $Pd_3Bi_2Se_2$.

II. METHODS

Single crystals of $Pd_3Bi_2Se_2$ were grown using the self-flux method. The starting materials, stoichiometric Pd powder (99.95%), Bi powder (99.99%), and Se powder (99.99), were mixed with excess Bi-Se (50% more by molar ratio), pressed into a pellet, and placed into an alumina crucible that was then sealed in a fused silica tube under a vacuum of ∼10 mTorr. The mixture was then heated to 610 °C and held for 24 h, slowly cooled to 500 °C at a rate of 1 C/h, and subsequently quenched to room temperature. Platelike single crystals with typical size $\sim 1.5 \times 1 \times 0.5$ mm^3 were obtained (see inset of Fig. S1 in the Supplemental Material [50]). The structure of the as-grown crystals was determined through single-crystal x-ray-diffraction (XRD) measurements (Bruker SMART APEX II, MoK_α radiation). Details of the structural refinement are provided in the Supplemental Material [50]. The orientation of larger single crystals was determined through XRD measurement using a PANalytical X'Pert Pro diffractometer with CuK_α radiation. X-ray diffraction shows that our samples of $Pd_3Bi_2Se_2$ crystallize in the monoclinic space group C2/*m* (No. 12) with refined lattice parameters $a = 11.7403(8)$ Å, $b = 8.4339(6)$ Å, $c = 8.4163(6)$ Å, and $\beta = 133.834(1)^\circ$, in good agreement with previous studies [47–49]. Electrical resistivity was measured using the standard four-probe technique in a Physical Properties Measurement System (PPMS-14T, Quantum Design) and in a dilution refrigerator (Bluefors) equipped with a 9–1–1 T triple-axis vector magnet. The TDO measurements were performed in a custom-built system operating at ∼14.5 MHz in a ^{3}He cryostat. In this technique, the change in the resonator frequency $\Delta f(T)$ is proportional to the change in magnetic susceptibility as $\Delta f(T) = -4\pi G \Delta\chi(T)$, where the geometrical factor G depends on the physical dimensions and geometry of the sample and resonator coil. In the Meissner state, the change in magnetic susceptibility reflects the change of the London penetration depth $\lambda(T)$ such that $\Delta f(T) \propto \Delta\lambda(T)$. The very small magnitude of the rf magnetic field (∼20 mG) ensures that the sample remains fully in the Meissner state during measurements. Magnetic torque measurements were performed using piezoresistive torque magnetometry with a 35-T resistive magnet at the National High Magnetic Field Laboratory in Tallahassee, Florida. The samples were mounted on self-sensing cantilevers that were placed in a ^{3}He cryostat. Measurements were performed with a balanced Wheatstone bridge that uses two piezoresistive paths on the cantilever, as well as two resistors at room temperature that can be adjusted to balance the circuit. The voltage across the Wheatstone bridge was measured using a lock-in amplifier (Stanford Research Systems, SR860).

The electronic structure of $Pd_3Bi_2Se_2$ was computed using DFT calculations. We employed the projector-augmented wave method as implemented in the Vienna *Ab initio* Simulation Package (VASP) within the generalized gradient approximation using the revised Perdew-Burke-Ernzerhof exchange-correlation functional for solids (PBEsol) [51,52]. Potentials for each atom were chosen corresponding to the following electron configurations: Bi ($5d^{10}\,6s^2\,6p^3$), Pd ($4d^9\,5s^1$), and Se ($4s^2\,4p^4$). First, optimization of the atomic positions, unit-cell shape, and unit-cell volume was performed on the primitive unit cell to a convergence level of 10^{-8} eV using an energy cutoff of 501 eV and including contributions from spin-orbit coupling and a Hubbard U correction for the Pd d states ($U_{Pd} = 2.19$ eV). Geometry and unit-cell parameters of the relaxed cell are given in Table S3 [50]. After relaxation, the charge density was first determined via a self-consistent calculation using a regular Γ-centered k-point mesh with the maximum distance between k points set to 0.1 Å^{-1}. The density of states was determined using the same k-point mesh, the Fermi surface was calculated using a Γ-centered mesh of 1000 k-points spanning the Brillouin zone, and the band structure was determined along high-symmetry k-point paths through the Brillouin zone. The C2X and XCRYS-

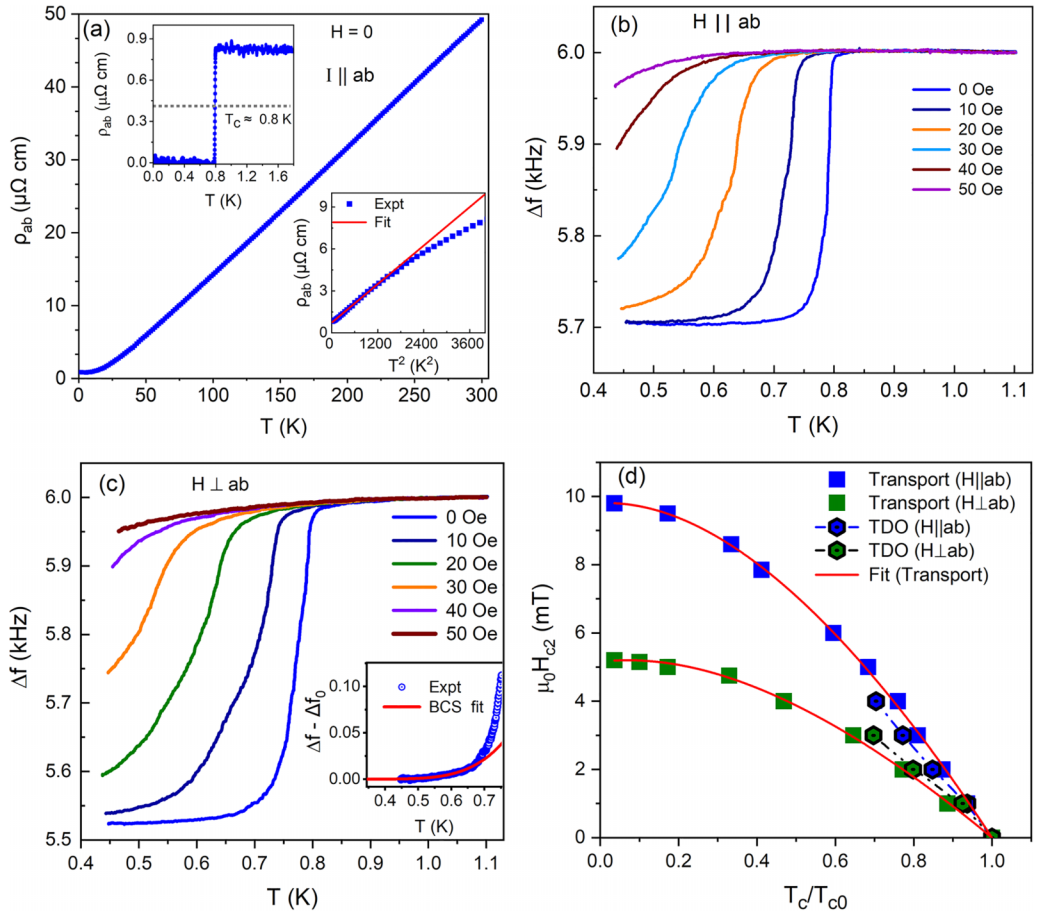

FIG. 1. (a) Temperature dependence of the electrical resistivity, $\rho_{ab}(T)$, of $Pd_3Bi_2Se_2$ measured between 300 and 1.8 K. The upper inset displays $\rho_{ab}(T)$ measured between 1.8 and 0.03 K. The horizontal dotted line represents the midpoint of the transition, used as a criterion for T_c. The lower inset shows ρ_{ab} vs T^2. The solid line is a fit of the form $\rho = \rho(0) + AT^2$. The temperature dependence of the TDO frequency shift between 0.4 and 1.1 K is shown as measured on a single crystal with $H||ab$ (b), and $H \perp ab$ (c). Inset: Zero-field data with BCS-like fit. (d) H_{c2} vs T superconducting phase boundaries in reduced temperature T_c/T_{c0} for both orientations and techniques. The solid lines are WHH model fits [57,58].

DEN software packages [53,54] were utilized to visualize the Fermi surface, and the band structure was visualized using the PYMATGEN PYTHON library. Calculations of cyclotron effective masses and dHvA frequencies were derived from the VASP output using in-house code.

III. RESULTS AND DISCUSSION

The main panel of Fig. 1(a) shows the temperature dependence of the in-plane electrical resistivity, $\rho_{ab}(T)$, of $Pd_3Bi_2Se_2$, measured between 300 and 1.8 K. $\rho_{ab}(T)$ exhibits typical metallic behavior, decreasing monotonically with temperature; $\rho_{ab}(1.8\ \text{K}) \approx 0.82\ \mu\Omega$ cm and the residual resistivity ratio (*RRR*), ρ_{ab} (300 K)/ρ_{ab} (1.8 K) ≈ 60. This *RRR* value is much larger than that reported earlier for polycrystalline [35] and thin-film samples [37], and combined with low residual resistivity, reflects the high quality of our single crystals. The upper inset of Fig. 1(a) displays $\rho_{ab}(T)$ between 1.8 and 0.03 K measured in a dilution refrigerator. Superconductivity is observed in the electrical resistivity with a $T_{c,\,\text{onset}}$ of ≈ 0.83 K, and zero resistance is reached at ≈ 0.78 K. Note that the T_c ≈ 0.80 K (defined as the midpoint of the transition) value of our single-crystal sample is slightly lower than that reported for a polycrystalline sample (≈ 0.95 K) [35]. The normal-state resistivity data can be fitted to $\rho_{ab}(T) = \rho_0 + AT^2$ below 40 K with $\rho_0 = 0.76\,\mu\Omega\,\text{cm}$ and $A = 2.2\,\text{n}\Omega\,\text{cm}\,\text{K}^{-2}$ [see lower inset of Fig. 1(a)]. The value of A falls within the range typically seen for correlated transition metals and A15-type superconductors [55,56]. The T^2 dependence of ρ_{ab} signals conventional Fermi-liquid ground state with dominant electron-electron scattering at low temperatures. $\rho_{ab}(T)$ above 40 K is approximately linear, reflecting dominant electron-phonon scattering at high temperatures.

The temperature dependence of the TDO frequency shift between 0.4 and 1.1 K measured on a single crystal under $H||ab$ is shown in Fig. 1(b). The sample displays superconductivity with the onset of the transition $T_c \approx 0.83$ K in zero field, which is consistent with the value observed in the electrical resistivity discussed above. With increasing field, the transition onset shifts to lower temperatures and is largely suppressed by 5 mT. As shown in Fig. 1(c), similar behavior is observed under $H \perp ab$. We attempt to analyze the zero-field temperature dependence TDO signal, $\Delta f(T)$. The solid line in the inset of Fig. 1(c) represents a fit of the data to the BCS

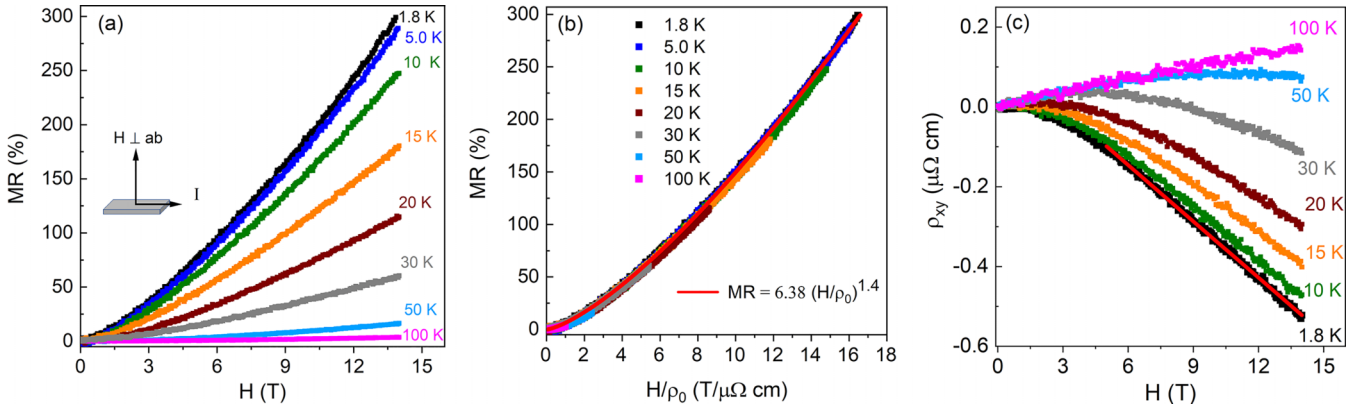

FIG. 2. (a) Transverse magnetoresistance of $Pd_3Bi_2Se_2$ at various temperatures. (b) Kohler scaling plot produced using the data in (a). Solid line (red) is a fit of the form $MR = 6.38[H/\rho(0)]^{1.4}$ to the data at 1.8 K. (c) Hall resistivity (ρ_{xy}) measured at various temperatures. Solid line (red) is a linear fit to the data at 1.8 K in higher-field regime (>5 T).

weak-coupling behavior. Although the accessible temperature range below T_c is too small for a complete analysis of the low-temperature variation of the TDO signal, the available data suggest that $\Delta f(T)$ saturates at low temperatures, indicative of an exponential temperature dependence of $\lambda(T)$ and a complete superconducting gap.

To construct the complete superconducting-phase diagram, we performed resistivity measurements in a dilution refrigerator following two protocols: with temperature sweep at fixed field and with field sweep at fixed low temperatures below T_c (shown in Fig. S3 [50]). From the data in Figs. 1(b) and 1(c) and Fig. S3, the superconducting-phase diagram is constructed as shown in Fig. 1(d) (see Ref. [50] for the detailed criteria used to estimate T_c and H_{c2}). A Werthamer-Helfand-Hohenberg (WHH) fit [56–58] to the data yields the upper critical field $\mu_0 H_{c2}(0) \sim 9.7$ mT for in-plane direction ($H||ab$) and $\mu_0 H_{c2}(0) \sim 5.3$ mT for out-of-plane direction ($H \perp ab$), and upper critical field slopes at T_c of -19.3 and -11.3 mT/K, respectively. The corresponding GL coherence lengths can be evaluated using the GL relations, yielding large coherence lengths of $\xi_{\text{out of plane}}(0) \approx 111$ nm and $\xi_{\text{in plane}}(0) \approx 190$ nm. We notice a modest anisotropy of the upper critical field, $H_{c2}^{ab}/H_{c2}^{c} \lesssim 2$, consistent with the three-dimensional Fermi surface observed through dHvA oscillation measurement and DFT calculation that we will discuss later. Our measured ξ exceeds that reported for polycrystalline samples (≈32 nm) [35] by more than a factor of 5 and is comparable to that of epitaxial thin films (≈140 nm) [37]. Such evolution is expected since the superconducting coherence length increases with increasing purity (*RRR*), that is, increasing electron mean-free path (l), as expressed by the dirty-limit relation $\xi \sim (l\xi_0)^{1/2}$, where ξ_0 is the BCS coherence length.

While there is no sign of any magnetic anomaly in $\rho_{ab}(T)$ [Fig. 1(a)], the electrical transport exhibits a large response to the application of a magnetic field. Figure 2(a) displays the transverse ($H \perp ab, I||ab$) magnetoresistance $MR = \frac{[\rho(H)-\rho(0)]}{\rho(0)}$ measured at various temperatures. The MR is positive at all temperatures and increases with decreasing temperature, reaching 300% at 1.8 K and 14 T, a value much larger than that reported for a thin-film sample [39]. For a system with either a single band (or a dominant single band) or multiple bands with electron-hole compensation, the transverse MR is expected to follow Kohler's scaling law [59,60], provided that electron transport can be described by a single-scattering time whose anisotropy does not change with temperature or field. In that case, all field- and temperature-dependent data collapse onto a single curve when plotted as MR versus $\frac{H}{\rho(0)}$ described by the equation $MR = \mathcal{F}[H/\rho(0,T)]$ [59,60]. Here, $\mathcal{F}$ is a scaling function that reflects the electronic band structure. For small values of the argument $\frac{H}{\rho(0,T)}$, the MR is typically quadratic, $MR \sim H^2$, while the high-field behavior depends on details of the electronic structure. In compensated materials, the MR keeps growing as H^2. In contrast, in uncompensated materials with all closed electron orbits, the MR in high fields saturates while open orbits induce saturation or an H^2 variation, depending on the details of the orbits. Polycrystalline samples, averaging over all types of orbits, display a linear high-field MR [61,62]. Figure 2(b) shows the magnetotransport data of our single-crystal $Pd_3Bi_2Se_2$ following Kohler's scaling rule remarkably well. As we will see, the DFT-calculated electronic band structures described below indicate multiple electron- and hole bands at the Fermi level. Therefore, the scaling property implies that magneto-transport is dominated by a single band and the overall dependence at 1.8 K is well described by $MR = 6.38[H/\rho(0)]^{1.4}$, represented by the solid line in Fig. 2(b). In fields up to 14 T, we do not observe any signs of saturation, although in a log-log plot (Fig. S4 [50]) the slope of MR vs H in high fields is seen to decrease from 1.7 at low $H/\rho(0)$ to 1.4.

Figure 2(c) shows the field dependence of the Hall resistivity (ρ_{xy}) of $Pd_3Bi_2Se_2$ at different temperatures. While ρ_{xy} varies linearly with H with a positive slope at high temperature and low field, a nonlinearity in $\rho_{xy}(H)$ gradually develops and becomes obvious above 7 T at 50 K, leading to a sign change at high H. Generally, a nonlinear Hall resistivity with a sign change indicates that electron and hole bands with unequal carrier concentrations and mobilities both contribute to transport [61]. Accordingly, we analyzed the magnetotransport data using the standard two-band model [61,62]. Even though this model contains extensive assumptions and simplifications, it is nevertheless useful for exploring trends in transport behavior. While the

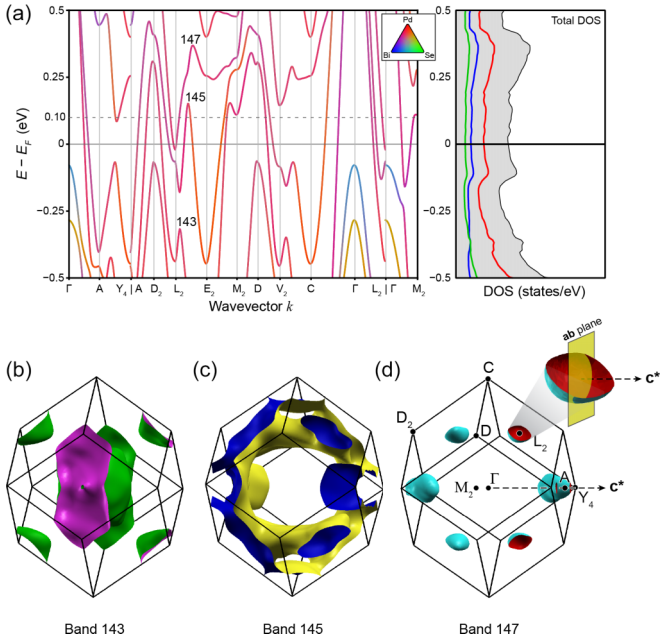

FIG. 3. (a) Electronic band structure and density of states (DOS) for $Pd_3Bi_2Se_2$ in the presence of spin-orbit coupling. The DOS from Pd (red), Bi (blue), Se (green), and the sum. Raising the Fermi level by 0.10 eV slightly expands the maximal orbit of the electron pocket at L_2, bringing it into alignment with the experimentally measured F_α. (b)–(d) Fermi surfaces corresponding to three doubly degenerate bands that cross the Fermi level presented in frame (a).

nonsaturating magnetoresistance following Kohler's scaling rule could indicate electron-hole compensation ($n_e = n_h$), the nonlinear sign-changing Hall resistivity is not consistent with compensation. Then, the limiting linear variation of ρ_{xy} at 1.8 K and high fields [red solid line in Fig. 2(c)] signals the approach to the high-field limit where the Hall coefficient (R_H) is given through $(n_h - n_e) = 1/eR_H = -1.3 \times 10^{22}$ cm^{-3}. Thus, this model predicts $n_e > n_h$ in the system. Together with the additional constraints given by the experimental values of the zero-field conductivity, $\sigma_0 = e(n_e\mu_e + n_h\mu_h)$, and the Hall resistivity, $\rho_{xy}/H = e(n_h\mu_h^2 - n_e\mu_e^2)/\sigma_0^2$, we deduce an overall charge density of order 10^{22} cm^{-3}. While this value is near the low end of electron concentrations typically seen in good metals, it is nevertheless consistent with the metallic behavior of $Pd_3Bi_2Se_2$ observed in the resistivity measurement [Fig. 1(a)]. However, we note that within the two-band ansatz, the approach to the high-field limit in ρ_{xy} and the simultaneous absence of saturation in ρ_{xx} in the same field range are inconsistent. We therefore conclude that the magnetotransport data in Fig. 2 cannot be accounted for within the two-band model in its standard form. One of the assumptions of this model relates to the absence of open orbits [60,61]. The inclusion of such orbits will, depending on their geometry, induce nonsaturating magnetoresistance and an additional contribution to the Hall resistivity, such that the standard relation with the carrier concentration is no longer valid [61–63], in agreement with our observed magnetotransport data.

To explore the possibility of open orbits, we performed DFT calculations of the electronic band structure of $Pd_3Bi_2Se_2$. The band structure presented in Fig. 3(a) reveals three pairs of doubly degenerate bands crossing the Fermi level. As shown in Figs. 3(b) and 3(c), bands No. 143 forms two large pockets centered at Γ and M_2, and band No. 145 consists of a complex continuous three-dimensional sheet. In particular, the Fermi surface sheet associated with band No. 145 supports the notion of open orbits in this system, with infinite channels running along both the a and c^* directions (Fig. S9 [50]). These open orbits may thus contribute to the observed magnetoresistance described above. Band No. 147 crosses the Fermi level (E_F) twice: once at the L_2 point of the Brillouin zone and again at a nonhigh-symmetry point along the path between Γ and Y_4. These crossings manifest as two closed-electron Fermi surface pockets in the Brillouin zone shown in Fig. 3(d). The bands associated with these electron pockets are highly dispersed and nearly parabolic close to E_F, so the resulting Fermi surface is very sensitive to the precise value of the Fermi energy [48]. For instance, with the magnetic field H oriented along c^* (perpendicular to the crystal layers), DFT yields a dHvA frequency of 14 T for the Fermi surface pocket at L_2. However, raising E_F by ∼0.10 eV [dashed line in Fig. 3(a)] enlarges the L_2 pocket and brings the calculated frequency in line with the experimental value ($F_\alpha \approx 145$ T).

In concert, a cyclotron effective mass of 0.15 m_0 (m_0 is the free-electron mass) is calculated, in good agreement with the measured $m^* = (0.11 \pm 0.02)m_0$, discussed later. The Fermi surfaces shown in Figs. 3(b), 3(c), and 3(d) are calculated using the shifted Fermi level, i.e., electron doping. A plausible source for such electron doping could be Se^{2-} vacancies introduced during synthesis [37,64]. Assuming a rigid-band model of the electronic structure, a shift of 0.10 eV amounts to 0.2 electrons per formula unit, corresponding to an ≈ 5% Se deficiency. Neither single-crystal x-ray diffraction (Table S2), energy-dispersive x-ray spectroscopy (Fig. S2), nor inductively coupled plasma spectroscopy (Table S4 [50]) reveals Se deficiency at this scale, although such nonstoichiometry may lie at the detection limit of these techniques. It should also be noted that the assumptions inherent to DFT may not precisely capture the nuances of the band structure near E_F, introducing a quantitative error in the estimated doping level. Further theoretical work and experimental validation are desirable for a comprehensive understanding of these discrepancies. Nevertheless, the angular dependence of our measured dHvA frequency (see below) and a good agreement with the cyclotron effective mass allow us to identify the L_2 pocket as the origin of F_α, as we will discuss in detail below.

To obtain experimental signatures of the Fermi surface of $Pd_3Bi_2Se_2$, we measured quantum oscillations using highly sensitive torque magnetometry at low temperatures and high magnetic fields up to 35 T. Figure 4(a) displays the field dependence of the magnetic torque, $\tau(H)$, measured at 0.5 K in a field applied approximately perpendicular to the ab plane (parallel to c^*) (also see Fig. S7 in the Supplemental Material [50]). dHvA oscillations are visible above ≈ 10 T. By subtracting a smooth polynomial background, we extract the oscillatory part of the magnetic torque, $\Delta\tau$, as shown in the inset of Fig. 4(a). Figure 4(b) shows $\Delta\tau$ plotted as a function of the inverse magnetic field (H^{-1}) at various temperatures, revealing the rapid suppression of the oscillation amplitude with increasing temperature. Nevertheless, the oscillations

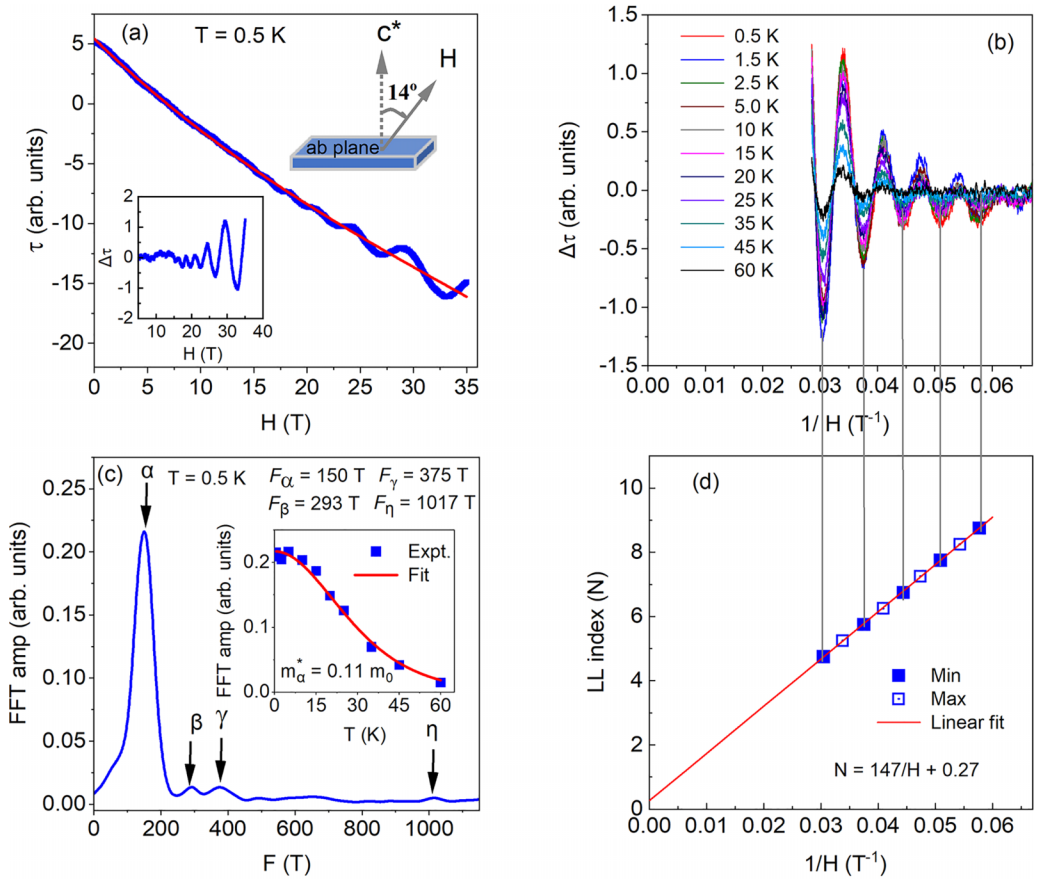

FIG. 4. (a) Field dependence of the magnetic torque τ (H) of $Pd_3Bi_2Se_2$ at 0.5 K. The field is applied at an angle $\boldsymbol{\theta} \sim 14^\circ$ from the c^* axis as depicted in the upper inset. This tilt angle was chosen for the temperature-dependent measurement as the oscillations are more pronounced at $\boldsymbol{\theta} \sim 14^\circ$, and is not far from the $H \perp ab$ plane [50]. The red curve is a third-order polynomial fit to the data. Lower inset: background-subtracted $\Delta\tau$ vs H. (b) $\Delta\tau$ plotted as a function of H^{-1} at various temperatures. (c) FFT amplitude as a function of frequency at 0.5 K. Inset: variation of FFT amplitude with temperature for the α band. The solid line is a fit with thermal damping term of Eq. (1). (d) Landau-level fan plot constructed for the dominating α band. The red line is a linear fit to the data.

persist up above 60 K, allowing us to determine the carrier cyclotron effective mass as discussed later. From the fast Fourier transform (FFT) performed in the field range of 15–35 T, four oscillation frequencies are identified as $F_\alpha = 150 \pm 26$ T, $F_\beta = 293 \pm 10$ T, $F_\gamma = 375 \pm 20$ T, and $F_\eta = 1017 \pm 12$ T, shown in Fig. 4(c) and Fig. S5 [50] with the low frequency dominating the spectrum. The error bars are determined by the half width at half height of the FFT peaks. The dominant frequency, $F_\alpha = 150$ T, occupies a small portion ($\approx 1.3\%$) of the total area of the primitive in-plane Brillouin zone of monoclinic $Pd_3Bi_2Se_2$.

The dHvA oscillations can be described by the Lifshitz-Kosevich formula [65,66]:

$$\Delta\tau \propto -\frac{1}{F}\frac{\partial F}{\partial \theta} H^{\lambda} R_T R_D R_S \sin\left[2\pi\left\{\frac{F}{H} - \left(\frac{1}{2} - \Phi\right)\right\}\right], \quad (1)$$

where F (in units of tesla) is the frequency of the oscillation, θ is the field angle, $R_T = \frac{A(\frac{m^*}{m_0})\frac{T}{H}}{\sinh(A(\frac{m^*}{m_0})\frac{T}{H})}$ is the thermal damping factor, $A = \frac{2\pi^2 k_B m_0}{e\hbar} = 14.7\text{T/K}$, $R_D = \exp(-A\frac{m^*}{m_0}\frac{T_D}{H})$ is the Dingle damping factor (T_D is the Dingle temperature), and $R_S = \cos(\pi g^* \frac{m^*}{2m_0})$ is the spin reduction factor (m^* is the cyclotron effective mass and g^* is the effective g factor). The exponent $\lambda = 1$ is chosen for a two-dimensional (2D) FS, and $\lambda = 3/2$ for a three-dimensional (3D) FS [67]. In addition, the phase factor, $\Phi = \frac{\Phi_B}{2\pi} + \delta$, where Φ_B is the Berry phase, and $\delta = 0$ for a 2D and $\pm 1/8$ for a 3D FS ($\pm$ sign corresponds to the minima (+)/maxima (−) of the cross-sectional area of the FS for the case of an electron band; for a 3D hole band, the sign of δ is opposite [68]. The quantum oscillation frequency is related to the area (S) of the extremal orbit through the Onsager relation, $F = (\frac{\hbar}{2\pi e})S$.

The temperature dependence of the FFT amplitude of the α band is displayed in the inset of Fig. 4(c). From a fit of the thermal damping factor R_T [defined in Eq. (1)] to these data, we obtain a light cyclotron effective mass of $m^*_\alpha = (0.11 \pm 0.02)m_0$. This is in good agreement with $m^*_\alpha = 0.15m_0$ derived from our DFT calculation, corroborating our assignment of the L_2 pocket as discussed earlier. Owing to their approximate 1:2 ratio, the F_β frequency ($F_\beta = 293$ T) may be the second harmonic of F_α. The amplitude of this oscillation frequency is too small to confirm this hypothesis by extracting an effective mass, which would be expected to be twice that of the fundamental mass m^*_α (i.e., $m^*_\beta = 0.22m_0$). Our DFT calculations reveal that the area of the electron

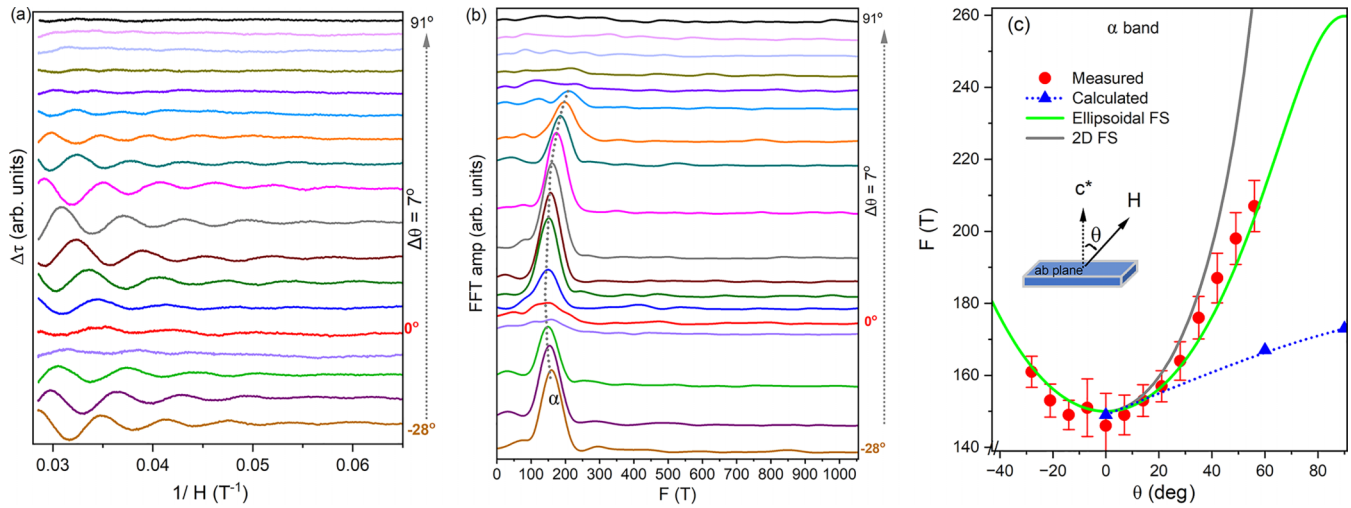

FIG. 5. (a) $\Delta\tau(H)$ vs H^{-1} of $Pd_3Bi_2Se_2$ measured at $T = 0.5$ K and at different angles θ [defined in the inset of (c)]. A vertical shift is added to the data for visual clarity. These data are obtained after subtracting a smooth background from the field-dependent torque data, $\tau(H)$ (Fig. S7 [50]). In the background-subtracted data, the change in frequency and the phase of the oscillations are more apparent. (b) The FFT spectrum obtained from the data in (a). The dashed line is a visual guide, indicating the progression of the α band. (c) Angular dependence of F_α measured (red). The error bars are taken as the half-width at half height of the FFT peaks. Solid lines represent 2D FS (gray), 3D ellipsoidal FS (green), and the DFT-calculated values (blue) as described in the text. Inset: sketch defining the field-angle direction.

pocket near Y_4 corresponds to a dHvA frequency of 289 T, providing an alternative explanation for the F_β frequency. Notably, the closed Fermi surface branches originating from band No. 143 produce dHvA frequencies greatly exceeding any of our measured values.

The field dependence of the oscillation amplitude at a given temperature can provide information about the Dingle temperature, T_D, through the analysis of Dingle plots (see Fig. S6 [50]). From T_D (≈ 37 K), the quantum relaxation time, τ_q, can be estimated through the relation $\tau_q = \frac{\hbar}{2\pi T_D k_B} = 0.32 \times 10^{-13}$ s, which, in turn, is proportional to the quantum mobility, $\mu_q = \frac{e\tau_q}{m^*} = 0.05$ m^2/V s. Additional parameters obtained from the analysis of the dHvA oscillations are listed in Table S5 [50]. Within the Drude model, the conductivity associated with the L_2 pockets can be estimated using the parameters obtained from the dHvA measurements as $\sigma = en\mu$, where μ is the mobility given above and n is the volume concentration [69] of electrons per L_2 pocket given as $n = \frac{2\sqrt{2}}{3\pi^2}(\frac{e}{\hbar})^{3/2} F_{\min}^{1/2} F_{\max} \approx 1.5 \times 10^{19}$ cm^{-3}, resulting in a resistivity of $\sim$395 μΩ cm for the two L_2 pockets in the Brillouin zone. Here, $F_{\min} \sim 116$ T and $F_{\max} \sim 260$ T are the minimum and maximum cyclotron frequency as determined within an ellipsoidal model from angular-dependent dHvA measurements as described below. Even though their mobility is high, the contribution of the L_2 pockets to the electric transport is small, chiefly because of their small size. These estimates suggest that magnetotransport is dominated by the large Fermi surface sheets shown in Figs. 3(b) and 3(c).

Phase analysis of the dHvA oscillations can reveal the topological properties of the associated carriers. For such analysis, the Berry phase can be extracted from the Landau-level (LL) fan diagram [5,65,67,70]. Since the dHvA spectrum is dominated by a single low-frequency (α band), the LL fan diagram can be constructed unambiguously without filtering the signal [71,72]. Since the magnetic torque is proportional to the density of states at the Fermi level [65,67], the LL fan diagram is constructed by assigning the oscillation minima in $\Delta\tau$ to $N - 1/4$ and maxima to $N + 1/4$, where N is the Landau-level index [65]. As shown in Fig. 4(d), $N(H^{-1})$ can be fitted with $N = 0.27 + 147/H$. The y axis intercept of the linear fit, following Eq. (1), yields the Berry phase as $\frac{\Phi_B^\alpha}{2\pi} \sim 0.4$, close to the value of 0.5 expected for a topological orbit. In this estimate, we used $\delta = -\frac{1}{8}$, appropriate for a 3D maximal electron orbit as discussed above. The slope of the linear fit corresponds to the frequency $F_\alpha = 147$ T, in good agreement with that obtained from the FFT spectra.

The Topological Materials Database [42,44–46] identifies $Pd_3Bi_2Se_2$ as a Z_2 topological material, which is characterized by a continuous direct gap at each k point in the Brillouin zone. The observed π phase would thus be consistent with the nontrivial topological nature of the α band. Furthermore, the Landau-level fan diagrams constructed for various angles reveal an angular dependence of the phase factor for the α band (Figs. S8(a) and S8(b) [50]), which may signal a topological phase transition [73–76]. Such interpretations should be taken with caution, however, as it has been noted that additional contributions to the phase shift of the quantum oscillations can arise from orbital momentum and Zeeman coupling [77]. Since these other contributions are presently not known for $Pd_3Bi_2Se_2$, a definite statement on the change of the topological state of the α band requires further studies.

The angular dependence of quantum oscillations can provide further information about the Fermi surface topology. Figure 5(a) displays $\Delta\tau$ (H) versus H^{-1} of $Pd_3Bi_2Se_2$ measured at $T = 0.5$ K for different angles θ [defined in the inset in frame 5(c)]. Upon the variation of θ, the dHvA oscillations change in both amplitude and peak position. Through FFT analysis, shown in Fig. 5(b), we can systematically track the dominant α band for various measured angles. Unfortunately,

the other bands could not be unambiguously tracked due to their much smaller amplitudes.

The FFT amplitude of the α band displays a distinct angular dependence such that for $\theta > 60^\circ$ it can no longer be identified unambiguously. Several factors may contribute to such angular variation. The torque technique introduces angular dependencies of the oscillation amplitude stemming from the fact that this technique probes the magnetization component that is transverse to the applied field direction. These are contained in the factor $\frac{1}{F}\frac{dF}{d\theta}$ in Eq.(1) [65], which for an ellipsoid is given as $-\frac{1}{F}\frac{dF}{d\theta} = -\frac{(1-\Gamma^2)\cos(\theta)\sin(\theta)}{\cos^2(\theta)+\Gamma^2\sin^2(\theta)}$, with $\Gamma = \frac{F_{\min}}{F_{\max}}$ the anisotropy of the dHvA frequency. This relation yields the expected vanishing torque at the symmetry points at $\theta = 0^\circ$ and $\theta = 90^\circ$, and a rapid decrease of the torque at angles larger than $\approx 60^\circ$. This drop becomes more precipitous; the larger the anisotropy is, the smaller Γ is. Furthermore, frequently a strong suppression of dHvA oscillations on layered materials is found for the in-plane field orientation [78,79]. A possible reason is related to the reduced electron mobility in the interlayer direction which would induce an increased Dingle temperature at large angle and the corresponding exponential suppression of the oscillations.

Figure 5(c) summarizes the angular dependence of F_α. The measured dHvA frequency increases symmetrically for positive and negative angles, implying that the FS pocket is symmetric about the plane spanned by the zero-angle field direction and the rotation axis. Referring to the geometry of the Brillouin zone in Fig. 3(d) and Fig. S10 [50], this finding is consistent with the a axis of the conventional base-centered monoclinic cell being the rotation axis. In k space, this axis corresponds to the Γ-M_2 direction. By the same reasoning, the Y_4 pocket has an irregular shape [see Fig. 3(d)] such that no rotation will yield a symmetric angular dependence of the oscillation frequency, excluding this pocket as the source of F_α. The observed increase of F_α with angle falls short of the $\frac{1}{\cos(\theta)}$ variation of a 2D FS but is consistent with a FS pocket in the shape of an ellipsoid. In fact, a fit for an ellipsoidal FS pocket aligned with the D-D_2 direction and rotated around the Γ-M_2 axis (Fig. 5(c) and Fig. S10 [50]) describes the data well with an anisotropy of $\Gamma \approx 0.45$. We note that the rotation axis is not aligned with a principal axis of the ellipsoid but subtends an angle of approximately 45°. Therefore, the minimum frequency is $F_{\min} \approx 116$ T, and not the frequency measured at $\theta = 0^\circ$, which is 145 T. Also included in Fig. 5(c) are the dHvA frequencies calculated using DFT with E_F shifted by ≈ 0.10 eV. While this calculation underestimates the angular dependence of F_α by approximately 20% at 60°, it qualitatively reproduces the monotonic increase in frequency with increasing θ.

IV. SUMMARY

In summary, we report on the growth of single-crystal samples of $Pd_3Bi_2Se_2$ and present their superconducting and normal-state magnetotransport properties. Superconductivity is observed in the electrical resistivity and TDO measurements, with a transition temperature at $T_c \approx 0.80$ K. The availability of large bulk single crystals enables the study of their anisotropic electronic properties. The samples are of high purity, as evidenced by a large residual resistivity ratio of ≈ 60 and the observation of dHvA oscillations in fields as low as 10 T. Our magnetoresistance data exhibit Kohler-type scaling behavior, with an unusual $H^{1.4}$ dependence, suggesting contributions from multiple bands, as reflected in the Hall resistivity with nonlinear field dependence. Through analysis of the observed dHvA oscillations, we identify four bands with frequencies of $F_\alpha = 150$ T, $F_\beta = 293$ T, $F_\gamma = 375$ T, and $F_\eta = 1017$ T. Among these bands, the α band (150 T) is the most dominant.

Angular-dependent dHvA measurements, in conjunction with DFT calculations, allow us to assign the α band to a nearly ellipsoidal electron pocket centered on the L_2 point of the Brillouin zone. The calculated dHvA frequency of the α pocket originating from band No. 147 can be aligned with our experimental results with an upward shift of the Fermi level by 0.10 eV, implying light electron doping of the sample by 0.2 electrons per formula unit. This ellipsoidal pocket displays modest anisotropy in the angular dependence of the dHvA oscillations. Lifshitz-Kosevich analysis of the dHvA oscillations reveals a small cyclotron effective mass $m^* = (0.11 \pm 0.02)m_0$ for this electron pocket, in good agreement with the value of $0.15m_0$ obtained from DFT calculations. The DFT calculations further reveal a large, three-dimensional extended Fermi surface sheet originating from band No. 145. This Fermi surface supports open orbits in the ab plane of the crystal and may account for the observed magnetotransport behavior and the overall low electronic anisotropy of $Pd_3Bi_2Se_2$. For instance, the anisotropy of the upper critical field measured in fields parallel and perpendicular to the ab planes is found to be less than 2. Landau fan diagrams constructed from the dHvA oscillations yield a nontrivial Berry phase for the dominant orbit, indicating nontrivial band topology. The nontrivial topology present in the bulk superconductor $Pd_3Bi_2Se_2$ makes it a promising candidate for exploring potential topological superconductivity.

ACKNOWLEDGMENTS

This work was supported by the U.S. Department of Energy (DOE), Office of Science, Basic Energy Sciences, Materials Sciences and Engineering. DFT calculations were performed using resources provided by the Center for Nanoscale Materials, a U.S. DOE Office of Science User Facility under Contract No. DE-AC02-06CH11357. DFT calculations presented here are based upon work supported by Laboratory Directed Research and Development (LDRD) funding from Argonne National Laboratory, provided by the Director, Office of Science, of the U.S. DOE under Contract No. DE-AC02-06CH11357. The energy-dispersive X-ray spectroscopy (EDX) measurement performed at the Center for Nanoscale Materials, a U.S. DOE, Office of Science User Facility, was supported by the U.S. DOE, Office of Basic Energy Sciences, under Contract No. DE-AC02-06CH11357. We thank Hengdi Zhao for help with the EDX measurements. A portion of this work was performed at the National High Magnetic Field Laboratory, Tallahassee which is supported by National Science Foundation Cooperative Agreement No. DMR-2128556 and the State of Florida.

[1] L. Fu, C. L. Kane, and E. J. Mele, Topological insulators in three dimensions, Phys. Rev. Lett. **98**, 106803 (2007).

[2] Y. L. Chen, J. G. Analytis, J.-H. Chu, Z. K. Liu, S.-K. Mo, X. L. Qi, H. J. Zhang, D. H. Lu, X. Dai, Z. Fang *et al.*, Experimental realization of a three-dimentional topological insulator, Bi_2Te_3, Science **325**, 178 (2009).

[3] Y. Xia, D. Qian, D. Hsieh, L. Wray, A. Pal, H. Lin, A. Bansil, D. Grauer, Y. S. Hor, R. J. Cava, and M. Z. Hasan, Observation of a large-gap topological-insulator class with a single Dirac cone on the surface, Nat. Phys. **5**, 398 (2009).

[4] X.-L. Qi and S.-C. Zhang, Topological insulators and superconductors, Rev. Mod. Phys. **83**, 1057 (2011).

[5] Y. Ando, Topological insulator materials, J. Phys. Soc. Jpn. **82**, 102001 (2013).

[6] L. Fu and C. L. Kane, Topological insulators with inversion symmetry, Phys. Rev. B **76**, 045302 (2007).

[7] C. Beenakker and L. Kouwenhoven, A road to reality with topological superconductors, Nat. Phys. **12**, 618 (2016).

[8] R. M. Lutchyn, J. D. Sau, and S. Das Sarma, Majorana Fermions and a topological phase transition in semiconductor-superconductor heterostructures, Phys. Rev. Lett. **105**, 077001 (2010).

[9] M. Sato and Y. Ando, Topological superconductors: A review, Rep. Prog. Phys. **80**, 076501 (2017).

[10] J. C. Y. Teo and C. L. Kane, Majorana Fermions and non-Abelian statistics in three dimensions, Phys. Rev. Lett. **104**, 046401 (2010).

[11] X.-L. Qi, T. L. Hughes, S. Raghu, and S.-C. Zhang, Time-reversal-invariant topological superconductors and superfluids in two and three dimensions, Phys. Rev. Lett. **102**, 187001 (2009).

[12] S. Deng, L. Viola, and G. Ortiz, Majorana modes in time-reversal invariant *s*-wave topological superconductors, Phys. Rev. Lett. **108**, 036803 (2012).

[13] Y. S. Hor, A. J. Williams, J. G. Checkelsky, P. Roushan, J. Seo, Q. Xu, H. W. Zandbergen, A. Yazdani, N. P. Ong, and R. J. Cava, Superconductivity in $Cu_xBi_2Se_3$ and its implications for pairing in the undoped topological insulator, Phys. Rev. Lett. **104**, 057001 (2010).

[14] M. P. Smylie, K. Willa, H. Claus, A. Snezhko, I. Martin, W.-K. Kwok, Y. Qiu, Y. S. Hor, E. Bokari, P. Niraula, A. Kayani, V. Mishra, and U. Welp, Robust odd-parity superconductivity in the doped topological insulator $Nb_xBi_2Se_3$, Phys. Rev. B **96**, 115145 (2017).

[15] L. A. Wray, S.-Y. Xu, Y. Xia, Y. S. Hor, D. Qian, A. V. Fedorov, H. Lin, A. Bansil, R. J. Cava, and M. Z. Hasan, Observation of topological order in a superconducting doped topological insulator, Nat. Phys. **6**, 855 (2010).

[16] J. L. Zhang, S. J. Zhang, H. M. Weng, W. Zhang, L. X. Yang, Q. Q. Liu, S. M. Feng, X. C. Wang, R. C. Yu, L. Z. Cao *et al.*, Pressure-induced superconductivity in topological parent compound Bi_2Te_3, Proc. Natl. Acad. Sci. USA **108**, 24 (2011).

[17] H. Takahashi, A. Sugimoto, Y. Nambu, T. Yamauchi, Y. Hirata, T. Kawakami, M. Avdeev, K. Matsubayashi, F. Du, C. Kawashima *et al.*, Pressure-induced superconductivity in the iron-based ladder material $BaFe_2S_3$, Nat. Mater. **14**, 1008 (2015).

[18] B. Jäck, Y. Xie, J. Li, S. Jeon, B. A. Bernevig, and A. Yazdani, Observation of a Majorana zero mode in a topologically protected edge channel, Science **364**, 1255 (2019).

[19] G.-H. Lee and H.-J. Lee, Proximity coupling in superconductor-graphene heterostructures, Rep. Prog. Phys. **81**, 056502 (2018).

[20] M. Masuko, M. Kawamura, R. Yoshimi, M. Hirayama, Y. Ikeda, R. Watanabe, J. J. He, D. Maryenko, A. Tsukazaki, K. S. Takahashi *et al.*, Nonreciprocal charge transport in topological superconductor candidate $Bi_2Te_3/PdTe_2$ heterostructure, npj Quantum Mater. **7**, 104 (2022).

[21] H. Yi, Y. F. Zhao, Y. T. Chan, J. Cai, R. Mei *et al.*, Interface-induced superconductivity in magnetic topological insulators, Science **383**, 634 (2024).

[22] M. S. Bahramy, O. J. Clark, B.-J. Yang, J. Feng, L. Bawden, J. M. Riley, I. Markovic, F. Mazzola, V. Sunko, D. Biswas *et al.*, Ubiquitous formation of bulk Dirac cones and topological surface states from a single orbital manifold in transition-metal dichalcogenides, Nat. Mater. **17**, 21 (2018).

[23] C. Xu, N. Wu, G-X. Zhi, B.-H. Lei, X. Duan, F. Ning, C. Cao, and Q. Chen, Coexistence of nontrivial topological properties and strong ferromagnetic fluctuations in quasi-one-dimensional $A_2Cr_3As_3$, npj Comput. Mater. **6**, 30 (2020).

[24] P. Zhang, Z. Wang, X. Wu, K. Yaji, Y. Ishida, Y. Kohama, G. Dai, Y. Sun, C. Bareille, K. Kuroda *et al.*, Multiple topological states in iron-based superconductors, Nat. Phys. **15**, 41 (2019).

[25] L. Fu and C. L. Kane, Superconducting proximity effect and Majorana fermions at the surface of a topological insulator, Phys. Rev. Lett. **100**, 096407 (2008).

[26] M. Mandal, N. C. Drucker, P. Siriviboon, T. Nguyen, A. Boonkird, T. N. Lamichhane, R. Okabe, A. Chotrattanapituk, and M. Li, Topological superconductors from a materials perspective, Chem. Mater. **35**, 6184 (2023).

[27] L. Jiao, S. Howard, S. Ran, Z. Wang, J. O. Rodriguez, M. Sigrist, Z. Wang, N. P. Butch, and V. Madhavan, Chiral superconductivity in heavy-fermion metal UTe_2, Nature (London) **579**, 523 (2020).

[28] H.-J. Noh, J. Jeong, E.-J. Cho, K. Kim, B. I. Min, and B.-G. Park, Experimental realization of Type-II Dirac Fermions in a $PdTe_2$ superconductor, Phys. Rev. Lett. **119**, 016401 (2017).

[29] F. Fei, X. Bo, R. Wang, B. Wu, J. Jiang, D. Fu, M. Gao, H. Zheng, Y. Chen, X. Wang *et al.*, Nontrivial Berry phase and type-II Dirac transport in the layered material $PdTe_2$, Phys. Rev. B **96**, 041201(R) (2017).

[30] T.-R. Chang, P.-J. Chen, G. Bian, S.-M. Huang, H. Zheng *et al.*, Topological Dirac surface states and superconducting pairing correlations in $PbTaSe_2$, Phys. Rev. B **93**, 245130 (2016).

[31] B. R. Ortiz, S. M. L. Teicher, Y. Hu, J. L. Zuo, P. M. Sarte, E. C. Schueller, A. M. Milinda Abeykoon, M. J. Krogstad, S. Rosenkranz, R. Osborn *et al.*, CsV_3Sb_5: A Z_2 Topological kagome metal with a superconducting ground state, Phys. Rev. Lett. **125**, 247002 (2020).

[32] S. D. Wilson and B. R. Ortiz, AV_3Sb_5 kagome superconductors, Nat. Rev. Mater. **9**, 420 (2024).

[33] T. Sakamoto, M. Wakeshima, Y. Hinatsu, and K. Matsuhira, Charge-density-wave superconductor $Bi_2Rh_3Se_2$, Phys. Rev. B **75**, 060503(R) (2007).

[34] U. S. Kaluarachchi, W. Xie, Q. Lin, V. Taufour, S. L. Bud'ko, G. J. Miller, and P. C. Canfield, Superconductivity versus structural phase transition in the closely related $Bi_2Rh_{3.5}S_2$ and $Bi_2Rh_3S_2$, Phys. Rev. B **91**, 174513 (2015).

[35] T. Sakamoto, M. Wakeshima, Y. Hinatsu, and K. Matsuhira, Transport properties in normal-metal $Bi_2Pd_3S_2$ and superconducting $Bi_2Pd_3Se_2$, Phys. Rev. B **78**, 024509 (2008).

[36] T. Sakamoto, M. Wakeshima, and Y. Hinatsu, Superconductivity in ternary chalcogenides $Bi_2Ni_3X_2$ (X = S, Se), J. Phys.: Condens. Matter **18**, 4417 (2006).

[37] J. Lapano, Y. Y. Pai, A. R. Mazza, J. Zhang, T. Isaacs-Smith, P. Gemperline, L. Zhang, H. Li, H. N. Lee, G. Eres *et al.*, Self-regulated growth of candidate topological superconducting parkerite by molecular beam epitaxy, APL Mater. **9**, 101110 (2021).

[38] M. Roslova, L. Opherden, I. Veremchuk, L. Spillecke, H. Kirmse, T. Herrmannsdörfer, J. Wosnitza, T. Doert, and M. Ruck, Downscaling effect on the superconductivity of $Pd_3Bi_2X_2$ (X = S or Se) nanoparticles prepared by microwave-assisted polyol synthesis, Inorg. Chem. **55**, 8808 (2016).

[39] Shama, D. Dixit, G. Sheet, and Y. Singh, Unusual Magneto-transport from two-dimensional Dirac Fermions in $Pd_3Bi_2Se_2$, Phys. E: Low-Dimens. **144**, 115457 (2022).

[40] Z.-T. Liu, C. Zhang, Q.-Y. Wu, H. Liu, B. Chen *et al.*, Charge density wave order and electron-boson coupling in ternary superconductor $Bi_2Rh_3Se_2$, Sci. China-Phys. Mech. Astron. **66**, 277411 (2023).

[41] E. Liu, Y. Sun, N. Kumar, L. Muechler, A. Sun, L. Jiao, S. Y. Yang, D. Liu, A. Liang, Q. Xu *et al.*, Giant anomalous Hall effect in a ferromagnetic kagome-lattice semimetal, Nat. Phys. **14**, 1125 (2018).

[42] Topological Materials Database, https://topologicalquantum-chemistry.org/#/, https://www.cryst.ehu.es/.

[43] B. Bradlyn, J. Cano, Z. Wang, M. G. Vergniory, C. Felser, R. J. Cava, and B. A. Bernevig, Beyond Dirac and Weyl fermions: Unconventional quasiparticles in conventional crystals, Science **353**, aaf5037 (2016).

[44] M. G. Vergniory, L. Elcoro, C. Felser, N. Regnault, B. A. Bernevig, and Z. Wang, A complete catalogue of high-quality topological materials, Nature (London) **566**, 480 (2019).

[45] B. Bradlyn, L. Elcoro, J. Cano, M. G. Vergniory, Z. Wang, C. Felser, M. I. Aroyo, and B. A. Bernevig, Topological quantum chemistry, Nature (London) **547**, 298 (2017).

[46] M. G. Vergniory, B. J. Wieder, L. Elcoro, S. S. Parkin, C. Felser, B. A. Bernevig, and N. Regnault, All topological bands of all nonmagnetic stoichiometric materials, Science **376**, 6595 (2022).

[47] Z. Zhang, M. Ikeda, M. Utsumi, Y. Yamamoto, H. Goto, R. Eguchi, Y. F. Liao, H. Ishii, Y. Takabayashi, K. Hayashi, and R. Kondo, Pressure dependence of the structural and superconducting properties of the Bi-based superconductor $Bi_2Pd_3Se_2$, Inorg. Chem. **63**, 2553 (2024).

[48] R. Weihrich, S. F. Matar, I. Anusca, F. Pielnhofer, P. Peter, F. Bachhuber, and V. Eyert, Palladium site ordering and the occurrence of superconductivity in $Bi_2Pd_3Se_{2-x}S_x$, J. Solid State Chem. **184**, 797 (2011).

[49] S. Seidlmayer, F. Bachhuber, I. Anusca, J. Rothballer, M. Bräu, P. Peter, and R. Weihrich, Half antiperovskites: V. Systematics in ordering and group-subgroup-relations for $Pb_2Pd_3Se_2$, $Bi_2Pd_3Se_2$, and $Bi_2Pd_3S_2$, Z. Kristallogr.- Cryst. Mater. **225**, 371 (2010).

[50] See Supplemental Material at http://link.aps.org/supplemental/10.1103/PhysRevB.110.075152 for the XRD and EDX spectra and structural and inductively coupled plasma-OES analysis (Tables S1, S2, S4), low-temperature transport data, Dingle plot, Landau fan diagrams, extended zone scheme highlighting the open orbits, and details of the ellipsoidal model. Additionally, DFT geometry for the primitive cell (Table S3) and various parameters obtained from dHvA oscillations (Table S4) are included.

[51] J. P. Perdew, A. Ruzsinszky, G. I. Csonka, O. A. Vydrov, G. E. Scuseria, L. A. Constantin, X. Zhou, and K. Burke, Restoring the density-gradient expansion for exchange in solids and surfaces, Phys. Rev. Lett. **100**, 136406 (2008).

[52] P. E. Blöchl, Projector augmented-wave method, Phys. Rev. B **50**, 17953 (1994).

[53] A. Kokalj, XCrySDen-a new program for displaying crystalline structures and electron densities, J. Mol. Graph. Model. **17**, 176 (1999).

[54] M. J. Rutter, C2x: A tool for visualisation and input preparation for Castep and other electronic structure codes, Comput. Phys. Commun. **225**, 174 (2018).

[55] A. C. Jacko, J. O. Fjarestadt, and B. J. Powell, A unified explanation of the Kadowaki-Woods ratio in strongly correlated metals, Nat. Phys. **5**, 423 (2009).

[56] R. Chapai, M. P. Smylie, H. Hebbeker, D. Y. Chung, W.-K. Kwok, J. F. Mitchell, and U. Welp, Superconducting properties and gap structure of the topological superconductor candidate Ti_3Sb, Phys. Rev. B **107**, 104504 (2023).

[57] T. Baumgartner, M. Eisterer, H. W. Weber, R. Flukiger, C. Scheuerlein, and L. Bottura, Effects of neutron irradiation on pinning force scaling in state-of-the-art Nb_3Sn wires, Supercond. Sci. Technol. **27**, 015005 (2014).

[58] N. R. Werthamer, E. Helfand, and P. C. Hohenberg, Temperature and purity dependence of the superconducting critical field, H_{c2}. III. Electron spin and spin-orbit Effects, Phys. Rev. **147**, 295 (1966).

[59] F. Duan and J. Guojun, *Introduction to Condensed Matter Physics*, Vol. 1 (World Scientific, Singapore, 2005).

[60] A. A. Abrikosov, *Fundamentals of the Theory of Metals* (North-Holland, Amsterdam, 1988).

[61] A. B. Pippard, *Magnetoresistance in Metals* (Cambridge University Press, Cambridge, 1989).

[62] C. M. Hurd, *The Hall Effect in Metals and Alloys* (Plenum, New York, 1972).

[63] S. Zhang, Q. Wu, Y. Liu, and O. V. Yazyev, Magnetoresistance from Fermi surface topology, Phys. Rev. B **99**, 035142 (2019).

[64] C. Coughlan, M. Ibanez, O. Dobrozhan, A. Singh, A. Cabot, and K. M. Ryan, Compound copper chalcogenide nanocrystals, Chem. Rev. **117**, 5865 (2017).

[65] D. Shoenberg, *Magnetic Oscillations in Metals* (Cambridge University Press, Cambridge, 2009).

[66] I. M. Lifshitz and A. M. Kosevich, The theory of magnetic susceptibility in metals at low temperatures, Sov. Phys. JETP **2**, 636 (1956).

[67] J. Hu, Z. Tang, J. Liu, X. Liu, Y. Zhu *et al.*, Evidence of topological nodal-line fermions in ZrSiSe and ZrSiTe, Phys. Rev. Lett. **117**, 016602 (2016).

[68] C. Li, C. M. Wang, B. Wan, X. Wan, H.-Z. Lu, and X. C. Xie, Rules for phase shifts of quantum oscillations in topological nodal-line semimetals, Phys. Rev. Lett. **120**, 146602 (2018).

[69] N. W. Ashcroft and N. D. Mermin, *Solid State Physics* (Holt, Rinehart & Winston, New York, 1976).

[70] R. Chapai, M. Leroux, V. Oliviero, D. Vignolles, N. Bruyant, M. P. Smylie, D. Y. Chung, M. G. Kanatzidis, W.-K. Kwok, J. F. Mitchell, and U. Welp, Magnetic breakdown and topology

in the Kagome superconductor CsV_3Sb_5 under high magnetic field, Phys. Rev. Lett. **130**, 126401 (2023).

[71] M. A. Khan, D. E. Graf, I. Vekhter, D. A. Browne, J. F. DiTusa, W. A. Phelan, and D. P. Young, Quantum oscillations and a nontrivial Berry phase in the noncentrosymmetric topological superconductor candidate BiPd, Phys. Rev. B **99**, 020507(R) (2019).

[72] R. Chapai, D. A. Browne, D. E. Graf, J. F. DiTusa, and R. Jin, Quantum oscillations with angular dependence in $PdTe_2$ single crystals, J. Phys.: Condens. Matter **33**, 035601 (2021).

[73] Z. J. Xiang, D. Zhao, Z. Jin, C. Shang, L. K. Ma, G. J. Ye, B. Lei, T. Wu, Z. C. Xia, and X. H. Chen, Angular-dependent phase factor of Shubnikov–de Haas oscillations in the Dirac semimetal Cd_3As_2, Phys. Rev. Lett. **115**, 226401 (2015).

[74] Y. Yang, H. Xing, G. Tang, C. Hua, C. Yao, X. Yan, Y. Lu, J. Hu, Z. Mao, and Y. Liu, Anisotropic Berry phase in the Dirac nodal-line semimetal ZrSiS: The effect of spin-orbit coupling, Phys. Rev. B **103**, 125160 (2021).

[75] J. Cao, S. Liang, C. Zhang, Y. Liu, J. Huang, Z. Jin, Z. G. Chen, Z. Wang, Q. Wang, J. Zhao, and S. Li, Landau level splitting in Cd_3As_2 under high magnetic fields, Nat. Commun. **6**, 7779 (2015).

[76] R. Chapai, P. V. Sreenivasa Reddy, L. Xing, D. E. Graf, A. B. Karki, T.-R. Chang, and R. Jin, Evidence for unconventional superconductivity and nontrivial topology in PdTe, Sci. Rep.**13**, 6824 (2023).

[77] A. Alexandradinata and L. Glazman, Fermiology of topological metals, Annu. Rev. Condens. Matter Phys. **14**, 261 (2023).

[78] K. W. Chen, G. Zheng, D. Zhang, A. Chan, Y. Zhu, K. Jenkins, F. Yu, M. Shi, J. Ying, Z. Xiang, X. Chen, Z. Wang, J. Singleton, and L. Li, Magnetic breakdown and spin-zero effect in quantum oscillations in kagome metal CsV_3Sb_5, Commun. Mater. **4**, 96 (2023).

[79] P. Li, Y. Wen, X. He, Q. Zhang, C. Xia, Z. M. Yu, S. A. Yang, Z. Zhu, H. N. Alshareef, and X. X. Zhang, Evidence for topological type-II Weyl semimetal WTe_2, Nat. Commun. **8**, 2150 (2017).